A new method for high-resolution imaging of Ku foci to decipher mechanisms of DNA double-strand break repair

Sébastien Britton,[1] Julia Coates,[1] and Stephen P. Jackson[1,2]

[1]The Wellcome Trust and Cancer Research UK Gurdon Institute, University of Cambridge, Cambridge, CB2 1QN, England, UK
[2]The Wellcome Trust Sanger Institute, Cambridge, CB10 1SA, England, UK

DNA double-strand breaks (DSBs) are the most toxic of all genomic insults, and pathways dealing with their signaling and repair are crucial to prevent cancer and for immune system development. Despite intense investigations, our knowledge of these pathways has been technically limited by our inability to detect the main repair factors at DSBs in cells. In this paper, we present an original method that involves a combination of ribonuclease- and detergent-based preextraction with high-resolution microscopy. This method allows direct visualization of previously hidden repair complexes, including the main DSB sensor Ku, at virtually any type of DSB, including those induced by anticancer agents. We demonstrate its broad range of applications by coupling it to laser microirradiation, super-resolution microscopy, and single-molecule counting to investigate the spatial organization and composition of repair factories. Furthermore, we use our method to monitor DNA repair and identify mechanisms of repair pathway choice, and we show its utility in defining cellular sensitivities and resistance mechanisms to anticancer agents.

Introduction

DNA double-strand breaks (DSBs) are the most toxic of all DNA lesions and are major mediators of cancer cell killing by radiotherapy and widely used chemotherapies (Jackson and Bartek, 2009). In addition to being generated by genotoxic chemicals and ionizing radiation (IR), DSBs arise as normal intermediates during V(D)J (variable diversity joining) and class switch recombination. Consequently, pathways dealing with DSBs are essential for both proper immune system development and preventing mutations or genome rearrangements that promote cancer (Ciccia and Elledge, 2010). Indeed, genes encoding DSB-responsive proteins are mutated in various hereditary human syndromes that often exhibit cancer predisposition, immunodeficiency, infertility, hypersensitivity to genotoxic agents, and/or developmental defects (Jackson and Bartek, 2009; Ciccia and

Elledge, 2010). DSB responses are also defective in certain cancer cells, thereby affecting their sensitivities to therapeutic agents (Jackson and Bartek, 2009).

Two main DSB repair pathways exist in mammals: homologous recombination (HR), which repairs a subset of radiation-induced DSBs in S and G2 phases of the cell cycle, and nonhomologous end joining (NHEJ), which repairs most radiation-induced DSBs irrespective of cell cycle status (Ciccia and Elledge, 2010). NHEJ is a robust and relatively rapid mechanism that joins DNA ends, thereby restoring chromosomal integrity (Mahaney et al., 2009; Lieber, 2010). NHEJ is initiated by DSBs being recognized by Ku, an abundant protein complex comprising heterodimerized Ku70 and Ku80 subunits, which contains a cavity that accommodates a DNA end (Walker et al., 2001). The Ku–DNA complex is then recognized by the DNA-dependent protein kinase (DNA-PK) catalytic subunit (DNA-PKcs), with the ensuing DNA-Ku–DNA-PKcs complex forming the active DNA-PK serine/threonine kinase (Dvir et al., 1993;

The Rockefeller University Press $30.00
J. Cell Biol. Vol. 202 No. 3   579–595
www.jcb.org/cgi/doi/10.1083/jcb.201303073

JCB   **579**

Figure 1. **Coupling RNase preextraction with high-resolution microscopy allows detection of NHEJ proteins at laser-induced DNA damage.** (A) Localizations of Ku80 and nucleolin were analyzed in undamaged U2OS cells by immunofluorescence without CSK (no CSK), with preextraction using CSK only (CSK), or CSK combined with RNase A (CSK+R). (B) Analysis by immunoblotting of NHEJ proteins in whole-cell extracts (WCE) and in fractions retained

Gottlieb and Jackson, 1993). Finally, DSB ligation is mediated by the DNA ligase IV–XRCC4–XLF complex.

Despite Ku being the main DSB sensor in mammalian cells, it has not hitherto been possible to visualize it at single DSB sites in cells by fluorescence microscopy (Bekker-Jensen et al., 2006; Polo and Jackson, 2011). Here, we show that this inability to detect Ku and other DNA repair proteins at DNA ends arises because a large fraction of these factors is associated with chromatin via RNA. We describe here a method that can easily be integrated with existing techniques and equipment, which combines RNase- and detergent-based preextraction with high-resolution microscopy, allowing detection of Ku and other NHEJ proteins at single DSBs in cells. To highlight the broad applications of this approach, we show how it can be combined with advanced microscopy techniques, such as super-resolution microscopy or single-molecule counting, to answer key questions regarding the mechanisms and control of DSB repair. In addition, we show that mechanisms uncovered by our approach can be exploited to sensitize cells to anticancer drugs and define cellular resistance mechanisms. We also discuss how RNase-based extraction and imaging may be useful in studying additional cellular processes wherein key proteins display affinities for both RNA and DNA.

Results

A method for visualizing NHEJ proteins at DSB sites

As Ku is the main DSB sensor in higher eukaryotes, we explored ways to monitor its loading on DNA ends in mammalian cells. By using indirect immunofluorescence, we observed that much Ku was still associated with nonextractable chromatin when undamaged human cells were treated with a mixture of detergent and sucrose known as cytoskeleton buffer (CSK; Fig.1 A), which is widely used to release soluble proteins before immunofluorescence staining (Cramer and Mitchison, 1995). Immunoblotting also revealed CSK-resistant retention of both Ku and DNA-PKcs, which contrasted with the NHEJ ligation proteins XRCC4 and XLF that were released by CSK treatment (Fig. 1 B). We hypothesized that Ku and DNA-PKcs retention might be mediated by RNA because Ku binds to specific RNAs, such as the human telomerase RNA component (Ting et al., 2005), and RNase treatment has been reported to improve detection of chromatin-associated NHEJ proteins by biochemical fractionation after treating cells with high doses of radiomimetic drugs (Drouet et al., 2005). Indeed, addition of RNase A to CSK (CSK+R) allowed extraction of virtually all Ku and DNA-PKcs as detected by immunoblotting, whereas it did not extract the histone variant protein H2AX (Fig. 1 B). Similarly, when CSK+R was used in immunofluorescence experiments, Ku was completely released from the nucleus along with the well-established RNA-associated protein nucleolin (Fig. 1 A, bottom). These data thereby established that a considerable proportion of Ku is associated with nuclear structures via RNA and suggested that this might mask detection of DSB-bound Ku.

To test whether CSK+R extraction allowed visualization of Ku at DNA damage sites, we first generated tracks of damage in cells by laser microirradiation (Bekker-Jensen et al., 2006) and visualized these with an antibody recognizing the serine-139 phosphorylated form of H2AX (γ-H2AX) that is generated within chromatin flanking DSB sites by the DNA damage–activated kinases ATM (ataxia telangiectasia mutated), ATR (ataxia telangiectasia and Rad-3 related), and DNA-PK (Rogakou et al., 1998). Despite us using high-resolution microscopy with deconvolution, Ku recruitment to γ-H2AX–associated DNA damage sites was faint and difficult to visualize, either with or without CSK preextraction (Fig. 1 C, top). Strikingly, the use of CSK+R to remove RNA-associated Ku revealed clear Ku accumulation at sites of laser microirradiation, essentially without detectable background staining (Fig. 1 C, bottom). Importantly, similar results were obtained with cells stably expressing GFP-tagged Ku70 or Ku80 (Fig. 1, D and E). This approach was not restricted to Ku because it also allowed us to readily detect DNA damage recruitment of other GFP-tagged NHEJ proteins, such as XRCC4 and XLF, that promote DSB ligation and polynucleotide kinase phosphatase that mediates DNA end processing (Fig. 1, F and G; and not depicted).

In accord with NHEJ proteins recognizing DNA termini in vitro, we found both Ku and XRCC4 to reside within "microfoci" along the laser tracks, which contrasted with a broader distribution of γ-H2AX that spreads away from DSB sites (Fig. 1 C, insets; Iacovoni et al., 2010). To determine whether the Ku being observed under these conditions was actually DNA bound, we generated a mutated Ku70 (Ku70-Mut6E) predicted to be defective in DNA binding but not altered in the overall architecture of the Ku70–Ku80 complex. This mutation was predicted to reverse the normally positive charge in the Ku cavity (Fig. S1 A) such that Ku70-Mut6E was unable to bind DNA in vitro (Fig. S1 B), despite it still being able to interact with Ku80 (Fig. S1 C). When we used siRNA depletion and complementation to replace endogenous Ku70 by GFP-tagged Ku70-Mut6E or wild-type Ku70 (Fig. S1 D), Ku70-Mut6E was still nuclear (Fig. S1 E) but was not detectably recruited to sites of laser irradiation, unlike the wild-type protein (Fig. S1 F). Together these data show that CSK+R extraction reveals Ku bound at DNA ends. Thus, CSK+R treatment allows visualization of Ku and other NHEJ proteins at cellular DSB sites.

after CSK extraction (−R) or CSK+R extraction (+R). (C) U2OS cells were microirradiated, postincubated for 5 min, and fixed without CSK or with preextraction using CSK or CSK+R. (D) Analysis by immunoblotting of expression levels of GFP-FLAG-Ku70 and GFP-FLAG-Ku80 in U2OS stable cells using antibodies against Ku70 and Ku80. (E) U2OS cells stably expressing GFP-FLAG-Ku70 (top) or GFP-FLAG-Ku80 (bottom) were microirradiated, postincubated for 5 min, and preextracted with CSK+R. Immunofluorescence was performed with an anti-GFP antibody. (F) Analysis by immunoblotting of GFP-FLAG-XRCC4 expression levels in U2OS stable cells with an antibody against XRCC4. (G) U2OS cells stably expressing GFP-FLAG-XRCC4 (clone 01) were microirradiated, postincubated for 5 min, and fixed without preextraction (top, no CSK) or preextracted with CSK+R (middle and bottom rows, CSK+R). In this figure, insets represent twofold zoom to highlight microfoci (boxed regions) formed by NHEJ proteins. The position of each nucleus, as defined by DAPI staining, is highlighted by a dotted line. Bars: (white) 10 µm; (green) 1 µm.
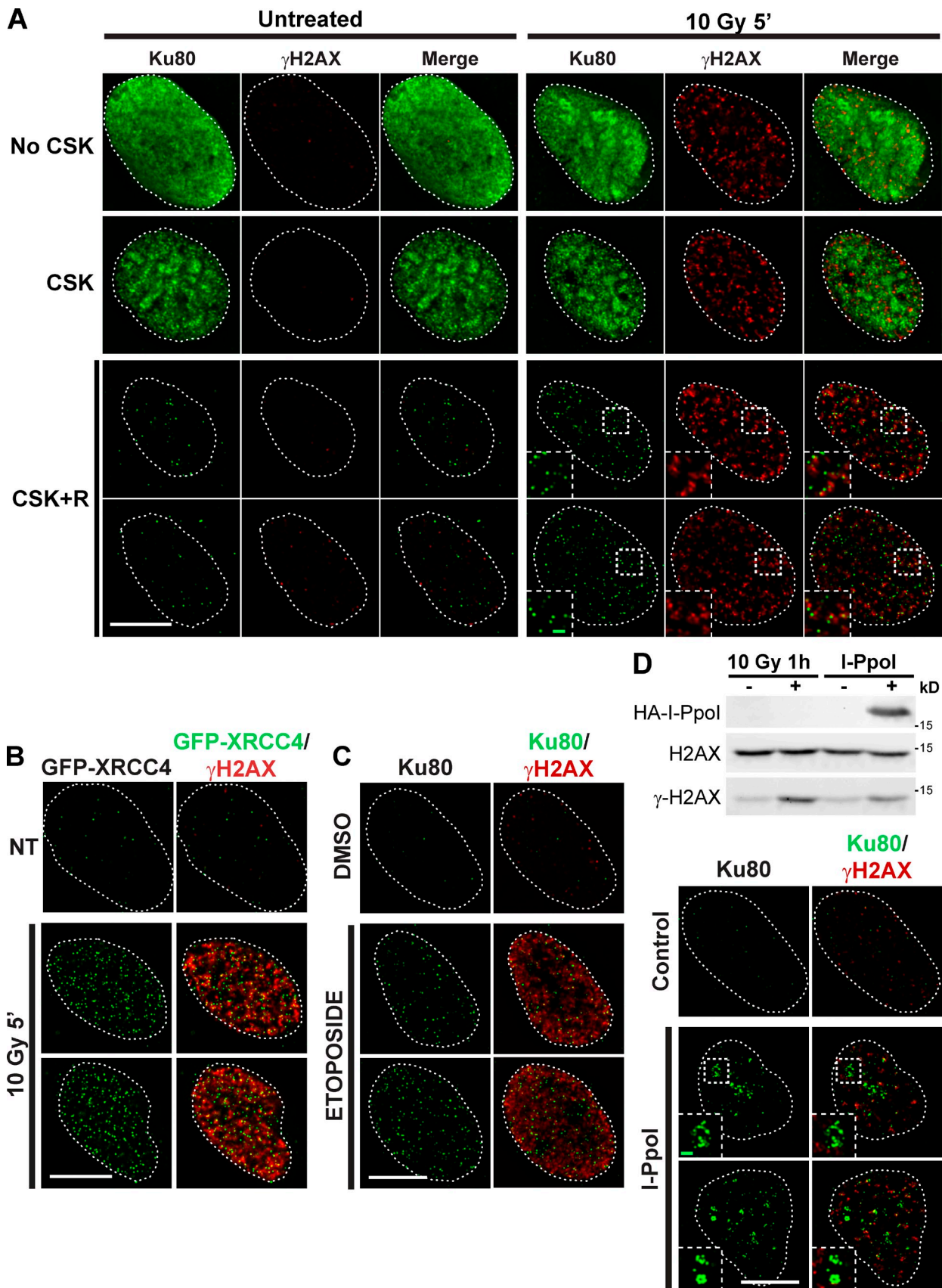
Figure 2. **The CSK+R extraction protocol reveals Ku at DNA ends generated by various DNA-damaging agents.** (A) U2OS cells were untreated (left columns) or irradiated with 10 Gy of IR (right columns), postincubated for 5 min, and fixed without CSK or with CSK or CSK+R preextraction. Quantifications of Ku foci generated 5 min after irradiation are provided in Fig. 5 A. (B) U2OS cells stably expressing GFP-FLAG-XRCC4 (clone 01) were untreated

DNA ends generated by carcinogens and anticancer agents are not generally "clean" but carry modifications such as protein–DNA adducts or damaged bases that must be processed by specific enzymes before DNA ligation (Mahaney et al., 2009; Weinfeld et al., 2011). To explore the range of applications for our approach, we tested whether it revealed Ku accumulation at various kinds of DNA ends, including those generated by IR or anticancer drugs. Upon treatment with IR, several genome surveillance proteins accumulate at sites of damage in foci known as IR-induced foci (IRIF). Strikingly, unlike existing techniques, CSK+R-based analyses allowed unprecedented detection of Ku IRIF in various human cell lines (Fig. 2 A and Fig. S2 A). With a lower dose of IR, we observed that most γ-H2AX IRIF contained one Ku IRIF, consistent with Ku IRIF forming at DNA ends (see Video 1 and Video 2 for 3D renderings of a whole U2OS nucleus and a single γ-H2AX focus, respectively). Some Ku IRIF not colocalizing with γ-H2AX could also be found (Video 1), which might correspond to Ku IRIF in regions of heterochromatin, where Ku IRIF could be observed (unpublished data) but that are refractory to H2AX phosphorylation (Kim et al., 2007). Importantly, Ku IRIF could be detected in all cell cycle phases including in mitosis (Fig. S2 B and not depicted), a cell cycle phase in which DNA repair is largely unexplored. Interestingly, GFP-tagged XRCC4 IRIF were also observed after CSK+R extraction, extending the applications of our approach to other NHEJ proteins (Fig. 2 B). Importantly, our approach also detected Ku at DNA ends generated after treating cells with etoposide, a topoisomerase II poison and anticancer agent (Fig. 2 C). Furthermore, CSK+R extraction enabled us to detect clusters of Ku foci in human cells expressing the rare-cutting site-specific nuclease I-PpoI (Fig. 2 D). Consistent with most accessible I-PpoI target sequences residing within arrays of tandem ribosomal DNA repeats in nucleoli (Berkovich et al., 2007), which are poorly chromatinized, we found that clustered I-PpoI–induced Ku foci were not associated with γ-H2AX staining (Fig. 2 E). Collectively, these findings indicated that CSK+R extraction and imaging readily detects the recruitment of NHEJ proteins at virtually any DSB, including those generated by IR and by drugs used in cancer therapy.

Importantly, CSK+R extraction did not detectably affect nuclear architecture or chromatin organization as judged by analyzing the nuclear lamina and regions of heterochromatin by anti–lamin A/C and anti-H3K9me3 (histone H3 K9 trimethyl) staining, respectively (Fig. S3, A and B). In addition, large IRIF of the DSB response mediator protein 53BP1 were not affected by CSK+R extraction (Fig. S3 C). Furthermore, visualization of laser-induced tracks of replication protein A and RAD51, which mark sites of HR events at early and late stages, respectively, was not impaired but was, in fact, somewhat enhanced by CSK+R

treatment (Fig. S3 D). Together, these data show that CSK+R extraction preserves the organization of the nucleus and of repair factories and is also compatible with analyzing HR events.

Super-resolution imaging of DNA repair complexes within chromatin

As each γ-H2AX focus appears to correspond to one DSB (Rogakou et al., 1999), γ-H2AX foci are frequently used to map locations of DSBs and to define positions of chromatin marks and repair complexes relative to DNA ends. In our high-resolution microscopy analyses, we observed that Ku foci are smaller than those of γ-H2AX (Fig. 2 A, insets; and Video 2), thereby suggesting that Ku IRIF would constitute more accurate markers of DSB localization. To test this, we combined CSK+R extraction with 3D structured illumination super-resolution microscopy (SIM), which provides a theoretical x-y resolution of ∼130 nm, as compared with 260 nm for conventional high-resolution microscopy (Schermelleh et al., 2008). With 3D-SIM, we observed that Ku foci were spherical in shape and with an apparent size of ∼170 nm (Fig. 3, A and B), which is significantly smaller than a typical γ-H2AX focus (∼600 nm; Bewersdorf et al., 2006; our data). Furthermore, with a complementary super-resolution method, stimulated emission depletion (STED), resolution in the x-y dimensions could be further increased (Fig. S4, A and B). Ku foci are therefore more precise markers of DSBs than γ-H2AX foci. During our experiments (Fig. 2 A), we sometimes observed two Ku foci in close proximity, suggesting that these might correspond to Ku loaded on each side of a single DSB. To test this, we used 3D-SIM and manually quantified the number of Ku foci per γ-H2AX focus. The ensuing frequency distributions indicated that, on average, there was only one Ku focus for each γ-H2AX focus (Fig. 3 C). These data therefore implied that, in the large majority of cases, each Ku focus contains both DNA ends associated with a DSB, thereby indicating that the process of DNA end bridging, called synapsis, is robust and must occur quickly after DSB induction (Soutoglou et al., 2007). Pairs of foci therefore likely reflect clustered DSBs that are often induced by IR (Ciccia and Elledge, 2010).

We next used γ-H2AX detection to explore whether our extraction and imaging procedures can define the organization of chromatin marks relative to DNA ends. Remarkably, in 3D-SIM images of irradiated cells, the staining patterns of Ku and γ-H2AX were mutually exclusive, with a central Ku focus in each case being flanked (nearly always on multiple sides) by larger, broader patterns of γ-H2AX staining (Fig. 3 D). To our knowledge, these data provide the first visual evidence that Ku localizes to DNA ends that are locally depleted of nucleosomes, with γ-H2AX being generated in the adjacent chromatin (Iacovoni et al., 2010).

(NT) or treated with 10 Gy of IR, postincubated for 5 min, preextracted with CSK+R, and processed for immunofluorescence with an anti-GFP antibody to boost the GFP signal. (C) U2OS cells were untreated (top row, DMSO) or treated for 30 min with 100 µM etoposide (middle and bottom rows) before being preextracted with CSK+R and processed for immunofluorescence. (D) U2OS Tet-On cells were transiently transfected with an empty plasmid (pICE; control) or with a plasmid expressing HA-I-PpoI (pICE-HA-NLS-I-PpoI; I-PpoI), and after 24 h, I-PpoI expression was induced by doxycycline for 5 h. Whole-cell extracts were collected and analyzed by immunoblotting (top), and cells on coverslips were preextracted with CSK+R and analyzed by immunofluorescence (bottom). In this figure, insets represent a twofold zoom to highlight Ku80 microfoci (boxed regions). The position of each nucleus, as defined by DAPI staining, is highlighted by a dotted line. Bars: (white) 10 µm; (green) 1 µm.
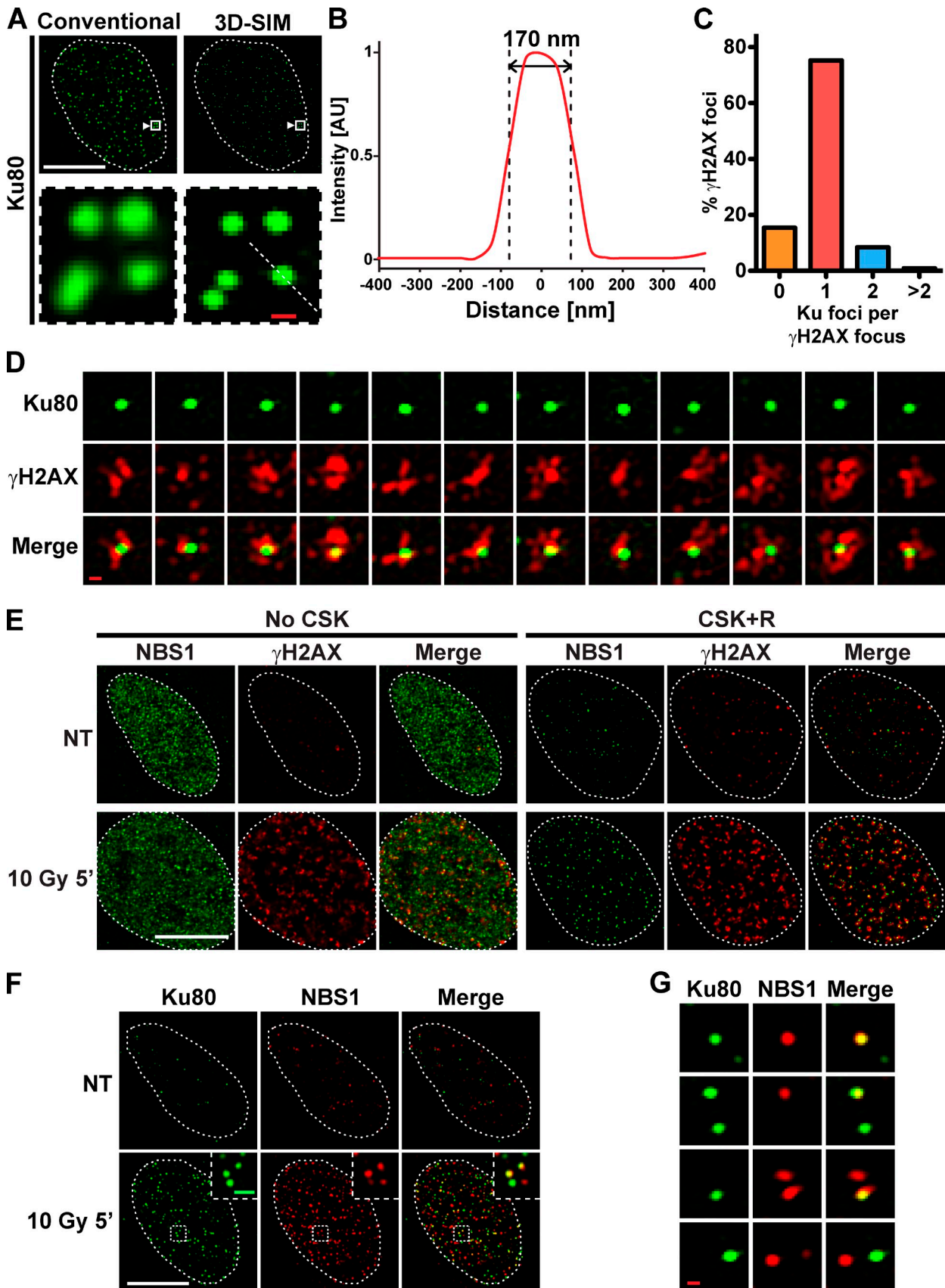
Figure 3. **CSK+R extraction allows super-resolution imaging of DNA damage sensors and chromatin marks at DNA ends.** (A) U2OS cells were treated with IR, postincubated for 5 min, preextracted with CSK+R, and processed for immunofluorescence. Cells were analyzed by high-resolution (top left, conventional) or SIM (top right, 3D-SIM). At the bottom, images are magnifications of the boxed regions highlighted by arrowheads in the top images,

Although it is well known that both Ku and the MRE11–NBS1–RAD50 (MRN) complex recognize DSBs (Ciccia and Elledge, 2010), it has until now remained unclear whether they can bind simultaneously to the same DNA end, whether they operate independently from one another, or whether one complex promotes or antagonizes binding of the other. We therefore addressed such issues by CSK+R extraction and super-resolution imaging. First, through using a specific anti-NBS1 antibody, we showed that CSK+R extraction markedly improved visualization of early NBS1 IRIF (Fig. 3 E). Using this antibody together with anti-Ku antibodies in CSK+R extraction-based imaging, we could simultaneously visualize Ku and NBS1 IRIF (Fig. 3 F). Notably, through use of 3D-SIM, we discovered that in many cases, Ku and MRN simultaneously occupied the same DNA damage site, and in these situations, the staining patterns for the two proteins colocalized (Fig. 3 G). In other cases, however, IRIF displayed staining for only one or the other protein, implying that Ku and MRN can also recognize DNA ends independently. What features (e.g., chromatin) determine whether a DSB is bound by Ku, MRN, or both can now be explored by further studies.

Single-molecule counting to address repair complex composition

The exact composition of repair complexes at DNA ends in cells is currently unknown. In the case of Ku, it has been shown in vitro that multiple Ku molecules can successively load on a single end of naked DNA and slide along the DNA molecule, finally covering it (de Vries et al., 1989). However, with a model chromatinized in vitro substrate, only one or two Ku molecules were able to load on a single DNA end (Roberts and Ramsden, 2007). To address whether and to what extent Ku binding might be restricted in cells, we used our new extraction and imaging procedures to define the number of Ku molecules within each IRIF by single-molecule counting (Ulbrich and Isacoff, 2007). This method comprises measuring the number of fluorescent molecules in a subcellular assembly by monitoring its fluorescence intensity during continuous imaging. Stochastic bleaching events of individual fluorophores will occur for each fluorescent molecule, and therefore, the number of bleaching steps before extinction corresponds to the number of fluorescent molecules in the complex (Fig. 4 A, theoretical fluorescence profiles). To apply this approach to Ku-containing repair complexes, we needed to generate a cell line in which all Ku molecules were homogeneously tagged with a fluorophore. Accordingly, we used recombinant adeno-associated virus (rAAV) to introduce,

by HR into human RPE-1 cells, a GFP tag after the start codon of each allele of the *XRCC6* gene that encodes Ku70 (Fig. 4 B). As seen by immunoblotting, by using this method, we isolated RPE-1 cells tagged on both *XRCC6* alleles (Fig. 4 C). Importantly, the tagged Ku70 protein was functional because it formed IRIF (Fig. 4 D), and the tagged cells behaved as wild-type cells in terms of IR sensitivity (Fig. 4 E). These cells were then used to evaluate the number of Ku molecules within each IRIF by monitoring bleaching events (Fig. 4 F, representative profiles). Strikingly, plotting the ensuing frequency distribution indicated that each Ku focus contains, on average, two Ku molecules, presumably loaded on each side of the DSB (Fig. 4 G). This number is in line with the small size of Ku foci (around or under 80 nm with STED; Fig. S4 B), which is compatible only with a maximum of six to eight Ku molecules per focus according to the size of each Ku dimer (Walker et al., 2001). These data therefore revealed that, although considerable numbers of Ku molecules can become threaded onto a single DNA end in vitro (de Vries et al., 1989), this is not the case when DSBs are generated within the physiological chromatin context. Mechanisms by which chromatin and associated proteins suppress excessive Ku loading—and the consequences of impairing such restriction mechanisms—can now be addressed by further studies using our extraction and imaging procedures.

Monitoring Ku foci as a readout of DNA repair

Although DSB-inducing genotoxic agents are used extensively in anticancer treatments, their utility is compromised by toxic effects on normal tissues. Much effort is being directed toward identifying, inducing, and exploiting repair defects in cancer cells (Jackson and Bartek, 2009), and consequently, there is considerable value to cancer research in developing more sensitive and versatile assays to monitor DNA repair. We hypothesized that repair could be assessed by using our extraction and imaging approach to measure the induction and rate of disappearance of Ku IRIF. Thus, we established a computer-based automated detection and quantification analysis of Ku foci and applied it to measure numbers of Ku foci in cells treated with increasing IR doses. This experiment validated the approach by yielding a linear relationship between Ku focus number and dose (Fig. 5 A). Moreover, posttreatment kinetics experiments revealed that Ku IRIF numbers peaked 5 min after irradiation and then decreased, after an exponential decay (Fig. 5 B). Accordingly, at 1 h after irradiation, the number of Ku IRIF was almost back to that seen

highlighting the resolution gain between high-resolution (bottom left) and super-resolution (bottom right) microscopy. (B) Graph showing the fluorescence profile, in arbitrary units (AU), of an individual 3D-SIM Ku focus, corresponding to the dashed line in the bottom right panel of A. The data shown are representative of 30 measured foci in two independent experiments. (C) Frequency distribution of the number of Ku foci per γ-H2AX focus. U2OS cells were treated with 2 Gy of IR, postincubated for 5 min, preextracted with CSK+R, and processed for immunofluorescence. 3D-SIM pictures were acquired and manually analyzed for Ku foci, as represented by a frequency distribution. The data shown are from a single representative experiment out of two repeats. For the experiment shown, *n* = 535. (D) Ku and γ-H2AX spatial distributions as analyzed by 3D-SIM. Representative 3D-SIM pictures analyzed in C are presented. (E) U2OS cells were untreated (NT) or treated with 10 Gy of IR, postincubated for 5 min, and analyzed by immunofluorescence for NBS1 or γ-H2AX, without CSK preextraction (no CSK) or with CSK+R preextraction. (F) U2OS cells were untreated (NT) or treated with 10 Gy of IR, postincubated for 5 min, preextracted with CSK+R, and processed for immunofluorescence. Insets represent initial and 3.3-fold magnifications from boxed regions. (G) U2OS cells were treated with 2 Gy of IR, postincubated for 5 min, preextracted with CSK+R, and processed for immunofluorescence. 3D-SIM pictures were acquired, and representative foci are presented. The position of each nucleus, as defined by DAPI staining, is highlighted by a dotted line. Bars: (white) 10 µm; (green) 1 µm; (red) 0.2 µm.
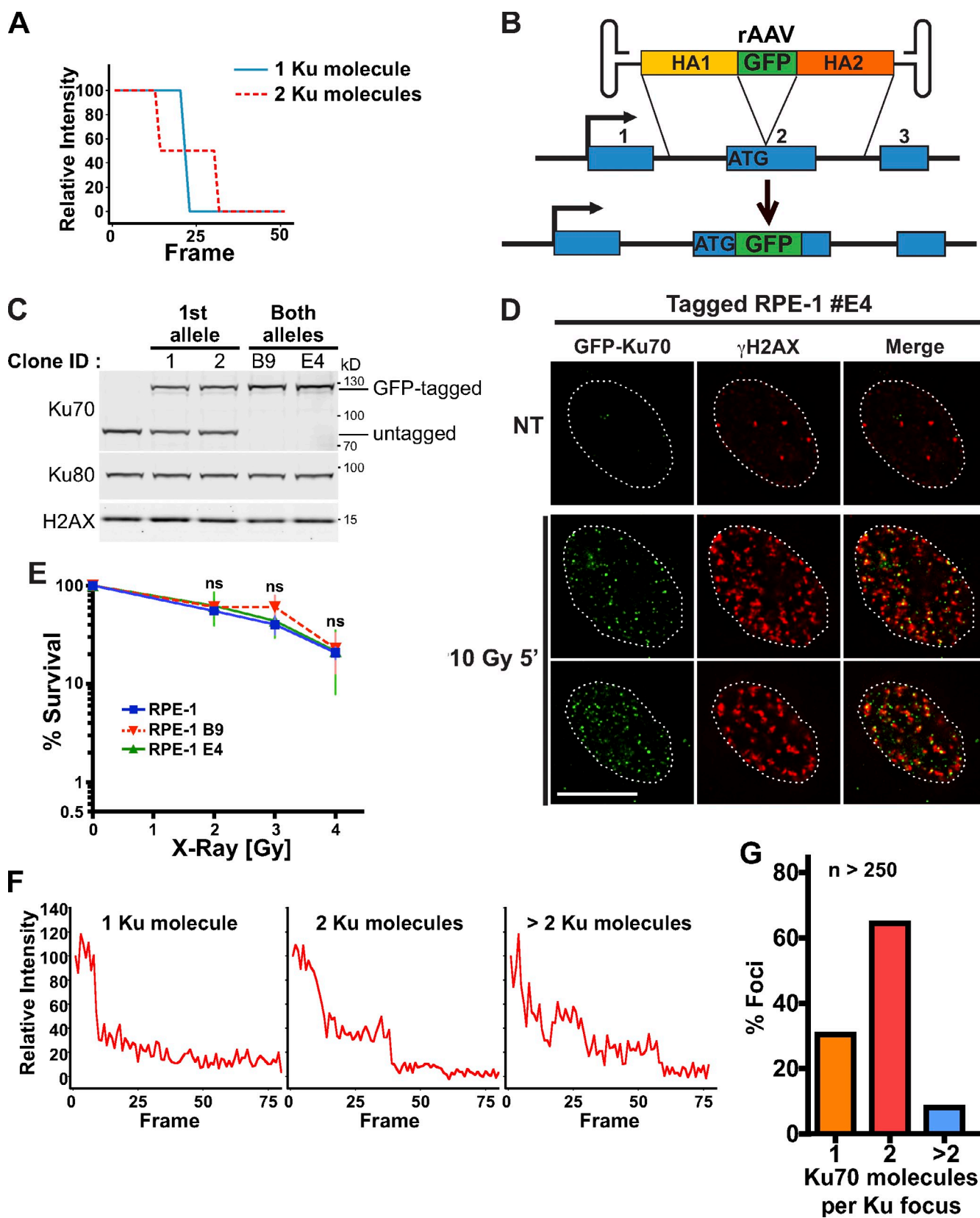
Figure 4. CSK+R extraction permits definition of repair complex composition by single-molecule counting. (A) Fluorescence intensity profiles of a hypothetical Ku focus, containing one or two molecules, plotted over several data acquisition frames. (B) Schematic representation of endogenous tagging of Ku70. RPE-1 cells were infected with an rAAV construct consisting of the GFP-FLAG sequence surrounded by two homology arms targeting HR after the start codon of the *XRCC6* (Ku70) gene. (C) Immunoblotting of extracts from untagged cells or cells tagged with GFP on one or both *XRCC6* alleles. (D) RPE-1 GFP tagged on both *XRCC6* alleles (clone E4) were untreated (NT) or treated with 10 Gy of IR, postincubated for 5 min, preextracted with CSK+R, and processed. The position of each nucleus, as defined by DAPI staining, is highlighted by a dotted line. Bar, 10 μm. (E) RPE-1 cells or two RPE-1
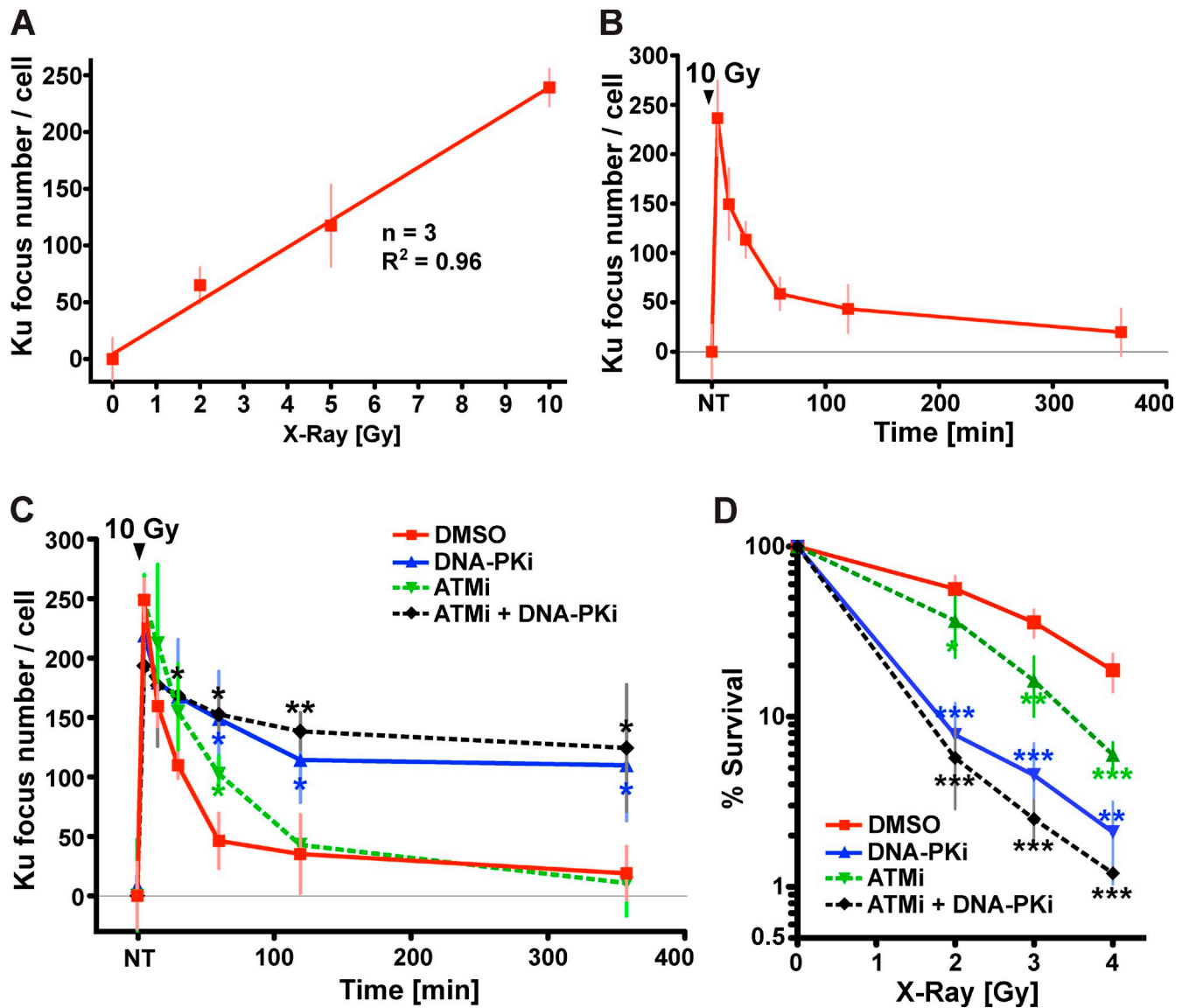
Figure 5. **CSK+R extraction allows assessment of DSB repair through software-assisted Ku focus quantification.** (A) Graph representing a dose–response analysis of the number of Ku foci 5 min after the indicated x-ray doses. U2OS cells were treated, postincubated for 5 min, preextracted with CSK+R, and processed. High-resolution pictures of >20 cells were acquired for each condition and submitted to automated focus detection by Volocity software. The slope given by linear regression of these data ($R^2 = 0.962$) equated to 24 Ku foci per Gy, which is less than the expected 30–40 DSBs per Gy per mammalian cell (Ciccia and Elledge, 2010). This apparent discrepancy might reflect some DSBs being blocked and unable to recruit Ku within the time frame of our experiments. Such blocks could represent certain DSBs possessing secondary structures or DNA base adducts, which must be removed for Ku to bind, and/or those residing within chromatin structures, which must be remodeled before Ku and other NHEJ components can gain access to the associated DNA ends. (B) Kinetic analysis of Ku IRIF numbers after 10 Gy of IR. U2OS cells were untreated (NT) or treated with 10 Gy of IR and postincubated for the indicated times. Cells were then processed and analyzed as in A. (C) Kinetic analysis of Ku IRIF numbers after 10 Gy of IR. U2OS cells were preincubated with DMSO, NU7441 (DNA-PKi), and/or KU55933 (ATMi) and then untreated (NT) or treated and analyzed as in B. (D) Impact of ATMi and/or DNA-PKi on survival after IR. U2OS cells were preincubated with DMSO, DNA-PKi, and/or ATMi and treated with the indicated IR doses. Inhibitors were washed away 18 h after treatment, and cell survival was determined by colony formation. For all graphs, each point corresponds to at least three independent experiments, vertical bars correspond to standard deviations, and asterisks indicate a significant difference to DMSO control (*, $P < 0.05$; **, $P < 0.01$; ***, $P < 0.001$).

cell clones (E4 and B9) GFP tagged on both *XRCC6* alleles were treated with the indicated IR doses, and their survivals were analyzed by clonogenic assay (ns indicates a nonsignificant difference to sensitivity of untagged RPE-1). (F and G) RPE-1 cells endogenously tagged on both *XRCC6* alleles (clone E4) were treated with 10 Gy of IR, postincubated for 5 min, preextracted with CSK+R, and processed. A small nuclear volume was continuously imaged, and fluorescence profiles of multiple individual foci were plotted to determine the number of bleaching steps for each focus. The data shown are from a single representative experiment out of two repeats. For the experiment shown, $n = 263$. (F) Representative fluorescence profiles analyzed in G of focus containing one, two, or more than two Ku molecules. (G) Numbers of bleaching steps, corresponding to the number of GFP-Ku70 molecules per focus, are represented as a frequency distribution.

Table 1. **Parameters describing exponential decay curves generated by nonlinear regression for each posttreatment kinetics**

Parameters	DMSO	DNA-PKi	ATMi	DNA-PKi + ATMi
Plateau ± SD (%)	10.71 ± 3.25	50.87 ± 8.79	4.56 ± 6.99	65.21 ± 8.31
Significance of difference to control	−	P < 0.01	ns	P < 0.001
Corresponding p-value	−	0.0018	0.2393	0.0005
Significance of difference to DNA-PKi	−	−	P < 0.01	ns
Corresponding p-value	−	−	0.002	0.1094
K ± SD	0.0436 ± 0.0057	0.0254 ± 0.0138	0.0178 ± 0.0036	0.0176 ± 0.0115
Significance of difference to control	−	ns	P < 0.01	P < 0.05
Corresponding p-value	−	0.103	0.0027	0.0248
Significance of difference to DNA-PKi	−	−	ns	ns
Corresponding p-value	−	−	0.4114	0.496
Half-life (minutes; ln(2)/K)	15.91	27.29	38.83	39.28
Regression R^2	0.9463	0.4856	0.8888	0.4073

For each condition, the number of Ku foci 5 min after IR was set to 100% and considered as t = 0 min. Nonlinear regressions were then applied using Prism v6.0b to generate curves fitting to a one-phase exponential decay using the formula %RemainingFoci(t) = (100 − Plateau) × exp(−K × t) + Plateau. Minus signs indicate not applicable. K, decay constant; ns, no significant difference.

in untreated cells. Similar responses were also observed for endogenous Ku80 and for GFP-tagged Ku70 or Ku80 after laser microirradiation (unpublished data).

These data were therefore in line with the kinetics of DSB repair as estimated by pulse-field gel electrophoresis (Wang et al., 2001) and by measuring γ-H2AX focus number over time (Shibata et al., 2011), highlighting how Ku focus detection can be readily used to monitor DSB repair in single cells. To illustrate the utility of this approach, we tested the impact on DNA repair of two small-molecule drugs, NU7441 (DNA-PK inhibitor [DNA-PKi]) and KU55933 (ATM inhibitor [ATMi]), that target the kinase activities of the DSB sensor proteins DNA-PK (Leahy et al., 2004) and ATM (Hickson et al., 2004), respectively. Having validated their specificity and activity (Fig. S5), we analyzed their impact on DNA repair by monitoring Ku focus numbers in cells after IR treatment (Fig. 5 C). Thus, we found that DNA-PKi caused a significant persistence of Ku IRIF, revealing that inhibiting DNA-PK activity prevents the repair of ~50% of Ku-associated DSBs induced by IR (Fig. 5 C and see Table 1 for regression parameters). In contrast, ATMi did not lead to Ku IRIF persistence but, instead, significantly increased the half-life of Ku foci, revealing that ATM enhances the rate but not extent of repair of IR-induced DNA breaks bound by Ku. Furthermore, combining the ATMi and DNA-PKi affected both the rate and the extent of repair, in accordance with independent functions (Fig. 5 C). Finally, by measuring the impact of the inhibitors on cell survival after IR, we found that the repair defect induced by DNA-PKi directly correlated with cellular sensitivity to killing by IR, whereas ATMi produced a considerably more moderate effect (Fig. 5 D). This approach to measure DNA repair can therefore be used to study mechanisms that control DNA repair and test strategies to sensitize cells to agents used in cancer treatment.

Monitoring Ku foci to decipher interplay between repair pathways

Although it is widely accepted that DSBs occurring during DNA replication are predominantly repaired by HR in mammalian cells (Arnaudeau et al., 2001), we do not know whether or how they are hidden from Ku, which has extremely high affinity for DNA ends and is known to both promote NHEJ and also inhibit other DNA transactions (Ono et al., 1996; Frit et al., 2000). To test whether Ku focus detection could provide insights into such phenomena, we used the anticancer agent camptothecin, which traps topoisomerase I cleavage complexes to yield singlestrand DNA breaks. These breaks are then converted to DSBs during S phase when they are encountered by replication forks. As a consequence, after camptothecin treatment, γ-H2AX induction is observed only in S-phase cells (Arnaudeau et al., 2001; Furuta et al., 2003). Interestingly, through using CSK+R extraction and imaging, we found that, despite generating large numbers of γ-H2AX foci in S-phase cells, camptothecin hardly induced any Ku foci above background levels (Fig. 6 A, left). Because we were able to detect IR-induced Ku foci in S-phase cells, including in cells pretreated with camptothecin (unpublished data), we concluded that the absence of Ku foci in camptothecin-treated cells reflected active mechanisms that protect replication-associated DNA ends from Ku loading. While exploring potential mechanisms for this suppression, we discovered that, when cells were cultured with camptothecin in the presence of ATMi, they now formed large numbers of Ku foci in S phase that localized closely with γ-H2AX foci (Fig. 6 A, right). By quantifying such Ku foci, we established that their accumulation was both ATM dependent and time dependent but was not markedly affected by DNA-PKi (Fig. 6 B). These data thereby established that ATM activity vigorously suppresses Ku loading at lesions induced when replication forks encounter stalled topoisomerase I complexes, likely to promote DNA repair by HR, and also highlighted how small-molecule inhibitors may be used to control the repair pathway choice.

To determine the potential functional role for ATM antagonizing Ku loading at camptothecin-induced DNA lesions, we explored the impact of Ku status on cell killing caused by camptothecin treatment. Because Ku inactivation itself kills proliferating human cells (Li et al., 2002), we used SV40-transformed embryonic fibroblasts derived from wild-type or $XRCC5^{−/−}$ mice ($XRCC5$ encodes for Ku80; Fig. 6 C; Taccioli et al., 1994; Nussenzweig et al., 1996). We found that, although Ku loss had
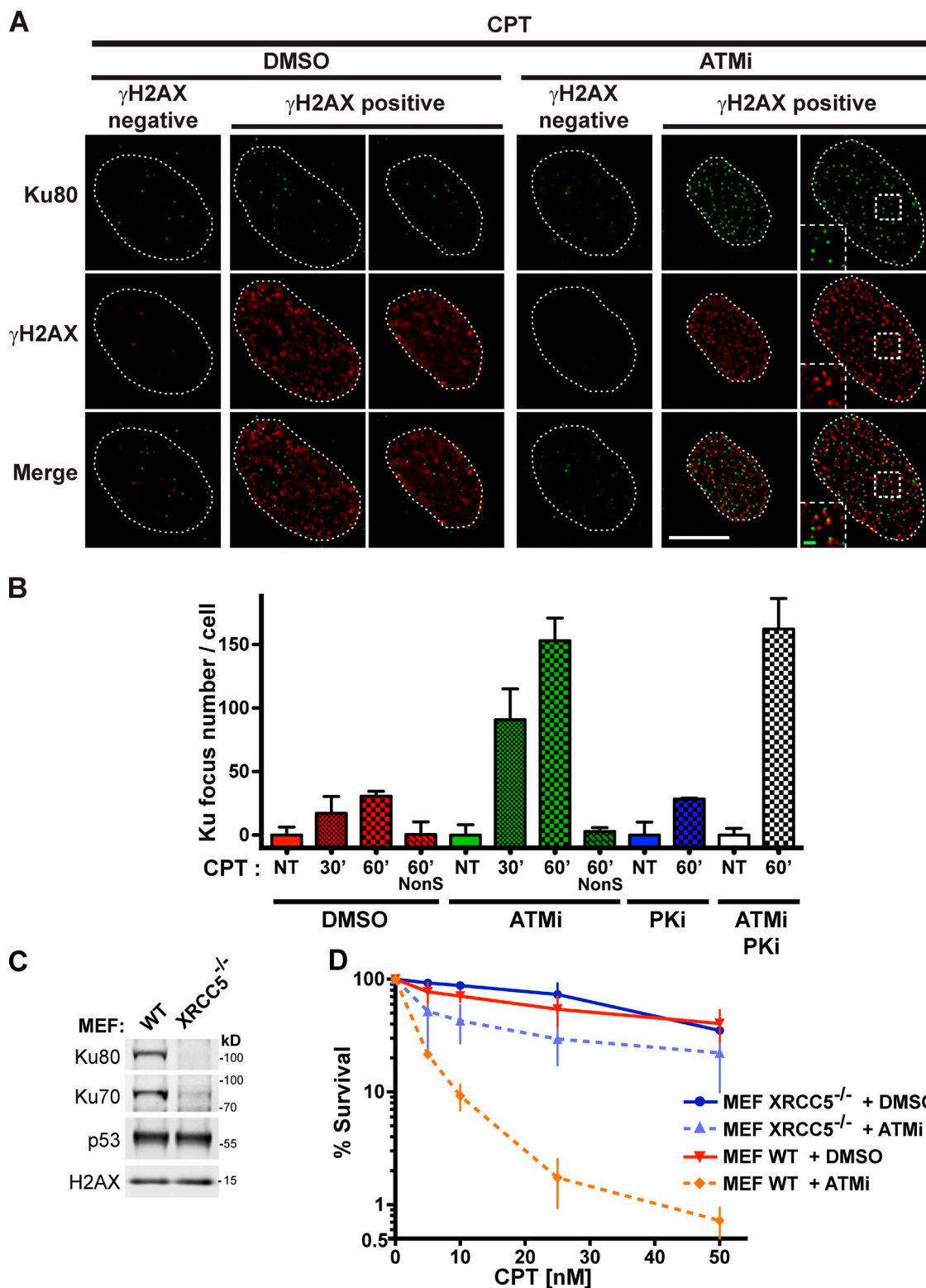
Figure 6. **CSK+R extraction enables observations into mechanisms controlling repair pathway choice.** (A) U2OS cells were preincubated for 1 h with DMSO or ATMi and then treated for 1 h with camptothecin (CPT) before being preextracted with CSK+R and processed for immunofluorescence. Cells in S phase were identified as showing pronounced γ-H2AX staining upon camptothecin treatment. The position of each nucleus, as defined by DAPI staining, is highlighted by a dotted line. Insets represent twofold zoom to highlight Ku80 microfoci (boxed regions). Bars: (white) 10 μm; (green) 1 μm. (B) U2OS cells were preincubated 1 h with DMSO, ATMi, and/or DNA-PKi before being treated with DMSO (NT, not treated) or 1 μM camptothecin for the indicated times (minutes). At the end of the treatment, cells were preextracted with CSK+R and processed for immunofluorescence. Ku foci were quantified as in Fig. 5 A in cells in S phase untreated or treated with camptothecin. NonS columns represent Ku focus numbers in non–S-phase cells treated for 1 h with CPT. Each bar corresponds to at least three independent experiments. (C) Total extracts from MEFs derived from wild-type (WT) or *XRCC5*^{−/−} mice were analyzed by immunoblotting. (D) MEF wild type or *XRCC5*^{−/−} were preincubated for 1 h with DMSO or 10 μM ATMi and then treated with the indicated doses of camptothecin. Inhibitors and camptothecin were washed away 18 h later, and cell survival was determined by colony formation. Each point corresponds to three independent experiments. Error bars correspond to standard deviations.

little or no effect on cell survival at the concentrations of campto-thecin we used, dramatic camptothecin sensitization was produced when wild-type ($XRCC5^{+/+}$) cells were cultured in the presence of ATMi (Fig. 6 D). Remarkably, this cell killing caused by camptothecin combined with ATM inhibition was almost entirely abrogated in Ku-deficient cells ($XRCC5^{-/-}$; Fig. 6 D). Collectively, these findings suggested that, when ATM is inhibited, Ku loads onto camptothecin-induced lesions, with ensuing toxicity being caused by Ku blocking DSBs from being channeled into HR pathways and/or through Ku triggering improper repair within the replication structures, leading to chromosomal fusions or translocations. These data highlighted how CSK+R extraction and imaging can be used to uncover mechanisms crucial for genome stability, how such mechanisms can be targeted to sensitize cancer cells toward therapeutic agents, and how down-regulation of Ku might provide a mechanism for therapy resistance.

Discussion

We have provided a simple, yet highly versatile, method—consisting of RNase-based preextraction combined with high- and super-resolution imaging techniques—that allows the isolation and study of DNA-associated functions of proteins and protein complexes that possess affinities for both DNA and RNA. Although we have applied this approach to study Ku and associated DNA repair factors, we speculate that related RNase-based extraction and imaging methods will prove useful in studying various other DNA damage signaling and repair pathways as well as events such as transcription, chromatin alterations, and telomere biology, wherein many protein complexes display affinities for both DNA and RNA.

To our knowledge, the CSK+R extraction–based approach that we have established is unique in that it combines the potential to perform in depth imaging and molecular characterization of Ku-based repair factories at single DSB sites in single cells, together with functional analyses of DNA repair. It also has broader applications, as it can be used with any human cell type (and likely with cells of many other species) to follow the associations of various repair proteins at single DNA ends. Finally, it is compatible with virtually all genotoxic agents that yield DSBs, including those used to treat cancer. Although we have applied this method to define mechanisms and control of DSB repair at DNA breaks generated by IR or topoisomerase I poisons, it will also enable future studies to interrogate cellular responses to various other experimental and clinical agents, such as topoisomerase II poisons and DNA cross-linkers.

In addition, by combining our approach with super-resolution microscopy, we have been able to study, with unprecedented detail, the spatial organization of the γ-H2AX chromatin mark and the MRN signaling/repair complex at and in the vicinity of single DSBs. Many studies are ongoing to identify and characterize the functions of chromatin marks induced at sites of damage and study the impact of chromatin status and nuclear architecture on DNA repair (Misteli and Soutoglou, 2009; Soria et al., 2012; Altmeyer and Lukas, 2013). We anticipate that our extraction and imaging approach will be useful in addressing

such topical issues. Furthermore, by combining CSK+R extraction with single-molecule counting, we also obtained information about the composition of repair complexes in cells and at the level of single molecules, establishing that there is generally one Ku focus containing two Ku molecules per DSB. Such studies in cells are unprecedented and pave the way for various additional ones, such as those designed to identify and investigate the mechanisms that limit Ku sliding and excessive Ku loading onto DSBs, and to determine what happens if such control mechanisms go awry. In this regard, we note that analysis of Ku foci can be used to define and characterize mechanisms that determine DNA repair pathway choice. Indeed, through addressing and highlighting such potential, we have found that loss of Ku activity, which has already been observed in some cancers (Perrot et al., 2012), could provide a mechanism for camptothecin resistance. Further imaging studies may provide additional insights into these findings, and could define further mechanisms for cancer cell sensitivity and resistance to experimental and therapeutic agents.

In addition to its wide applications in defining the spatial organization of DNA repair and associated signaling complexes, the approach that we have established also constitutes a new assay to study DNA repair at the single-cell level. The broad potential of this methodology is highlighted by the fact that another assay, the visualization and quantification of γ-H2AX foci, has become widely used to monitor DNA repair (Shibata et al., 2011), despite important limitations. First, in contrast to Ku foci, γ-H2AX foci do not form in poorly chromatinized regions (e.g., nucleoli) or in heterochromatin that is resistant to H2AX phosphorylation and/or dephosphorylation (Kim et al., 2007). Second, as for any phosphorylation, γ-H2AX induction and its disappearance can be affected by interference with its attendant kinases and phosphatases, meaning that, unlike Ku foci, it cannot always be taken as a reliable marker for DSB induction and repair. Finally, γ-H2AX can be induced by chromatin changes in the apparent absence of DSB formation (Bakkenist and Kastan, 2003), whereas this is unlikely to be the case for Ku foci. In light of these issues, we anticipate that the detection of Ku foci will provide more accurate and reliable readouts than current strategies based on γ-H2AX quantification.

Materials and methods

Cell culture
Cells were grown in a 5% CO_2 humidified incubator at 37°C. U2OS, U2OS Tet-On, HT1080, and SV40-transformed mouse embryonic fibroblasts (MEFs) derived from wild-type and $XRCC5^{-/-}$ mice (Nussenzweig et al., 1996) were grown in DMEM supplemented with 10% FBS, 2 mM L-glutamine, 100 U/ml penicillin, and 100 µg/ml streptomycin. $XRCC5^{-/-}$ MEFs have a 3.4-kb deletion of the Ku80 locus including the first two exons and a part of the promoter. RPE-1 human telomerase reverse transcriptase cells were grown in DMEM/Ham's F12 medium supplemented as in this paragraph and buffered with sodium bicarbonate.

DNA damage and drug treatments
Inhibitors were preincubated for 1 h before genotoxic treatments. ATMi (KU55933) and DNA-PKi (NU7441), both obtained from Tocris Bioscience, were used at 10 and 3 µM, respectively. For inducing protein expression with pICE, doxycycline (Takara Bio Inc.) was added at 2 µg/ml 2 d before treatment unless stated otherwise. Camptothecin (Sigma-Aldrich) was used at 1 µM except when stated otherwise. X-ray irradiations were

Table 2. **List of antibodies used in this study**

Target	Mono/polyclonal	Clone/reference	Antibody raised in	Source	Dilution for I.B.	Dilution for I.F.
53BP1	Polyclonal	NB100-304	Rabbit	Novus Biologicals	–	1:800
β-ACTIN	Monoclonal	8226	Mouse	Abcam	1:5,000	–
CHK1	Monoclonal	G4	Mouse	Santa Cruz Biotechnology, Inc.	1:100	–
CHK1 PhS345	Monoclonal	133D3	Rabbit	Cell Signaling Technology	1:1,000	–
CHK2	Polyclonal	ab8108	Rabbit	Abcam	1:2,000	–
CHK2 PhT68	Polyclonal	2661	Rabbit	Cell Signaling Technology	1:500	–
DNA-PKcs	Monoclonal	18.2	Mouse	Thermo Fisher Scientific	1:200	–
Fibrillarin	Monoclonal	AFB01	Mouse	Universal Biologicals	–	1:200
GFP	Polyclonal	A11122	Rabbit	Life Technologies	–	1:2,000
GFP	Monoclonal	7.1 + 13.1	Mouse	Roche	1:2,000	–
H2AX	Polyclonal	ab11175	Rabbit	Abcam	1:4,000	–
γ-H2AX	Polyclonal	2577	Rabbit	Cell Signaling Technology	1:500	1:100
γ-H2AX	Monoclonal	JBW301	Mouse	EMD Millipore	–	1:1,000
H3K9me3	Polyclonal	ab8898	Rabbit	Abcam	–	1:500
HA tag	Monoclonal	12CA5	Mouse	Home made	1:2,000	–
KAP-1	Polyclonal	ab10483	Rabbit	Abcam	1:5,000	–
KAP-1 PhS824	Polyclonal	IHC-00073	Rabbit	Bethyl Laboratories, Inc.	1:200	–
Ku70	Monoclonal	N3H10	Mouse	Abcam	1:200	–
Ku80	Monoclonal	111	Mouse	Thermo Fisher Scientific	1:2,000	1:100
Ku80 (for MEF)	Polyclonal	C-20	Goat	Santa Cruz Biotechnology, Inc.	1:100	–
Lamin A/C	Polyclonal	N-18	Goat	Santa Cruz Biotechnology, Inc.	–	1:200
NBS1	Polyclonal	NB100-143	Rabbit	Novus Biologicals	1:1,000	1:700
Nucleolin/C23	Polyclonal	H-250	Rabbit	Santa Cruz Biotechnology, Inc.		1:100
p53	Monoclonal	1C12	Mouse	Cell Signaling Technology	1:900	–
PCNA	Polyclonal	ab18197	Rabbit	Abcam	–	1:1,000
RAD51	Polyclonal	H-92	Rabbit	Santa Cruz Biotechnology, Inc.	–	1:200
RPA2/RPA32	Monoclonal	9H8	Mouse	Abcam	1:750	1:250
XLF	Polyclonal	ab33499	Rabbit	Abcam	1:500	–
XRCC4	Polyclonal	ab145	Rabbit	Abcam	1:2,000	–

Minus signs indicate that the antibody was not used for this application in this study. PCNA, proliferating cell nuclear antigen; I.B., immunoblotting; I.F., immunofluorescence.

performed with a calibrated irradiation system (RX-650; Faxitron) fitted with a 0.5-mm aluminum filter for soft x rays. Standard 10-Gy irradiation required an exposure time of 8 min and 33 s. Cells were irradiated in medium.

siRNA transfections

siRNA transfections were performed with Lipofectamine siRNAMAX (Life Technologies) according to the manufacturer's instructions. In brief, transfections were performed in 6-well plates containing 60% confluent cells, in 1.8 ml DMEM, 5% FBS, and 2 mM glutamine to which 200 µl of the transfection mix in Opti-MEM (Life Technologies) was added to a final concentration of 50 nM siRNA in the medium. 5 h after transfection, media were refreshed with DMEM, 10% FBS, and 2 mM glutamine. Transfections were repeated 24 h later to achieve optimal depletion. Posttransfection time for optimal depletion was 120 h after the second transfection for Ku70. Sense sequences for control (anti–Firefly luciferase) and anti-Ku70 siRNA are 5′-CGUACGCGGAAUACUUCGAdTdT-3′ and 5′-GAGUGAAGAU-GAGUUGACAdTdT-3′, respectively.

Antibodies

A list of antibodies with details and dilutions is provided in Table 2.

Immunoblotting

Total cell extracts were prepared by scraping cells in SDS lysis buffer (SLB; 4% SDS, 20% glycerol, and 120 mM Tris-HCl, pH 6.8), boiling for 5 min at 95°C, and 10 strokes through a 25-gauge needle. Absorbance at 280 nm was measured (NanoDrop; Thermo Fisher Scientific) to determine protein concentration, and lysates were diluted to 5 µg/µl in SLB. Before loading, lysates were diluted to 2.5 µg/µl with a solution of 0.01% bromophenol blue and 200 mM DTT and boiled for 5 min at 95°C. Proteins were resolved by SDS-PAGE and transferred onto nitrocellulose membrane (Protran; Whatman). Membranes were stained with Ponceau S to confirm homogeneous loading and cut into stripes, which were probed using the appropriate primary (Table 2) and appropriate donkey secondary antibodies coupled to IRDye 800CW (LI-COR Biosciences). Detection was performed with an imager (Odyssey; LI-COR Biosciences). Blots were cropped using PowerPoint (Microsoft).

Immunofluorescence

Cells were seeded on 160-µm-thick coverslips (VWR International) 24 h before experiments. After treatments, cells were washed with PBS and fixed for 15 min with 2% PFA in PBS before being washed three times with PBS. To preextract U2OS, cells were washed with PBS and then incubated twice for 3 min at room temperature with CSK buffer (10 mM Pipes, pH 7.0, 100 mM NaCl, 300 mM sucrose, and 3 mM MgCl₂) containing 0.7% Triton X-100 (CSK) and 0.3 mg/ml RNase A when specified (CSK+R). After preextraction, cells were washed with PBS and fixed with 2% PFA. To preextract RPE-1, the same protocol as for U2OS was used, but washes after preextraction were omitted and fixation was performed with 2% PFA in CSK without detergent instead of PBS. Before staining, cells were permeabilized for 5 min with PBS/0.2% Triton X-100, washed with PBS, and blocked with PBS/0.1% Tween 20 (PBS-T) containing 5% BSA. Coverslips were incubated for 1 h with primary antibodies in PBS-T/5% BSA and then washed with PBS-T and incubated with appropriate goat secondary antibodies coupled to Alexa Fluor 488 or 594 fluorophores (Life Technologies) in PBS-T/5% BSA. After washes in PBS-T and PBS, coverslips were incubated 30 min with 2 µg/ml DAPI in PBS. After washes in PBS, coverslips were dipped in water and mounted on glass slides using ProLong Gold (Life Technologies) specifically for STED microscopy or Vectashield (Vector Laboratories) mounting media for other experiments.

DNA manipulations

All plasmids generated in our work are deposited in Addgene together with annotated sequences. All constructs were validated to be mutation free by DNA sequencing. A list of DNA oligonucleotides used in this study is provided in Table 3. To generate pAAV-MCS2, a 1,345-bp fragment of

ID	Sequence 5′ to 3′	Restriction sites
FLAG-S	GATCTGATTACAAGGATGACGACGATAAGCTCGAGGGCGGCCGCGGAA	BglII, XhoI, NotI, and HindIII
FLAG-AS	AGCTTTCCGCGGCCGCCCTCGAGCTTATCGTCGTCATCCTTGTAATCA	BglII, XhoI, NotI, and HindIII
Ku70-F	CCGCTCGAGTCAGGGTGGGAGTCATATTACAAAACC	XhoI
Ku70-R	GGCGGATCCTTAGTCCTGGAAGTGCTTGGTGAGG	BamHI
Ku80-F	GGCCTCGAGGTGCGGTCGGGGAATAAGG	XhoI
Ku80-R	CGCGGATCCTATCATGTCCAATAAATCGTCCACATCACC	BamHI
XRCC4-F	CCGCTCGAGGACTACAAGGACGATGACGACAAGGGATCC	XhoI
XRCC4-R	GGCGAATTCTTAAATCTCATCAAAGAGGTCTTCTGG	EcoRI
AAVMCS-F	CGCGCGGCCGCGCTAGCGAATTCGCAGCTGTTGTGCTGTGTATGG	NotI, NheI, and EcoRI
AAVMCS-R	CGCGGGCCCACGCGTGGATCCCATCAACAGCATTCAACTGTGCC	BamHI, MluI, and Bsp12OI
Ku70-HA1-F	CGCGCGGCCGCGAAGACTGCTTGGTGAATTCTGGAGTTCGG	NotI
Ku70-HA1-R	GCCGCTAGCCATGTTGGCTACTGCTCACTAGGCG	NheI
Ku70-GFP-F	GCCGCTAGCAAGGGCGAGGAGCTGTTCACCG	NheI
Ku70-GFP-R	GGCACCGGTCTTATCGTCGTCATCCTTGTAATCAG	AgeI
Ku70-HA2-F	CCGACCGGTTCAGGGTGGGAGTCATATTACAAAACC	AgeI
Ku70-HA2-R	CCGACGCGTCAGTGAACCGAGATTGAGTCAGTGC	MluI
GFP-F	GGCAAGCTTACCGGTCGCCACCATGGTGAGCAAGGGCG	HindIII and AgeI
GFP-R	CCGCTCGAGCTTATCGTCGTCATCC	XhoI
Ku70siR-R	GGCACGCGTGCGGCCGCTTAGTCCTGGAAGTGCTTGGTGAGG	MluI and NotI
Ku70Mut6E1-R	GCTCTATTGGAGGAGGTTCGAGAGCCTTCTGGACCAGATTATAAATGC	—
Ku70Mut6E2-F	GGTCCAGAAGGCTCTCGAACCTCCTCCAATAGAGCTCTATCGG	—
Ku70Mut6E2-R	GGAGGGATGTTCCTCTCGGGTGTGTATCTGCACAATGCTGC	—
Ku70Mut6E3-F	GCAGATACACACCCGAGAGGAACATCCCTCCTTATTTTGTGGC	—

Minus signs indicate that the oligonucleotide does not contain any restriction site used for cloning.

Ku80 cDNA was amplified by PCR using AAVMCS-F and AAVMCS-R primers, digested with NotI–Bsp12OI, and cloned as a linker flanked by restrictions sites into NotI-digested pAAV-MCS (Agilent Technologies). pEGFP-C1-FLAG was generated by cloning annealed FLAG-S and FLAG-AS oligonucleotides in BglII–HindIII-digested pEGFP-C1 (Takara Bio Inc.). To generate pAAV-Ku70-TC, regions 21,406,712–21,408,580 and 21,408,581–21,410,371 of human chromosome 22 (RefSeq positions) were each amplified by PCR from RPE-1 genomic DNA using Ku70-HA1-F and Ku70-HA1-R and Ku70-HA2-F and Ku70-HA2-R primer pairs, respectively, giving HA 1 and HA 2 (homology arms 1 and 2). GFP-FLAG was amplified by PCR from pEGFP-C1-FLAG using Ku70-GFP-F and Ku70-GFP-R primers. HA1, GFP-FLAG, and HA2 PCR products were digested with NotI–NheI, NheI–AgeI, and AgeI–MluI restriction enzymes, respectively, and cloned into pAAV-MCS2 digested with NotI–MluI, yielding pAAV-Ku70-TC. To yield pEGFP-C1-FLAG-Ku70, pEGFP-C1-FLAG-Ku80, and pEGFP-C1-FLAG-XRCC4, respective cDNAs were amplified by PCR using Ku70-F/Ku70-R, Ku80-F/Ku80-R, and XRCC4-F/XRCC4-R primer pairs and, respectively, pEGFP-C1-6×His-Ku70 (Miller et al., 2010), pBABE-Puro-Ku80 (Falck et al., 2005), and XRCC4 isoform 2 cDNA (gift from P. Calsou, Centre National de la Recherche Scientifique, Toulouse, France) as templates. The resulting PCR products were digested with XhoI–BamHI, XhoI–BamHI, and XhoI–EcoRI, respectively, and cloned into pEGFP-C1-FLAG digested with the same enzymes. pICE is a new synthetic plasmid conferring puromycin resistance and allowing doxycycline-inducible expression of cDNAs. A plasmid containing an siRNA-resistant form of Ku70 cDNA (Ku70siR; Cheng et al., 2011) was given by P. Frit (Centre National de la Recherche Scientifique, Toulouse, France). Ku70siR cDNA was fused to GFP-FLAG and cloned into pICE by amplifying GFP-FLAG using GFP-F and GFP-R primers and pEGFP-C1-FLAG as a template and amplifying Ku70siR by using Ku70-F and Ku70siR-R primers. GFP-FLAG and Ku70 PCR products were digested with HindIII–XhoI and XhoI–MluI, respectively, and cloned into pICE digested with HindIII–MluI, giving pICE-EGFP-FLAG-Ku70siR-WT. For the K282E K287E T300E K331E K338E R403E mutant (Mut6E), region 847–1,212 of Ku70 cDNA carrying the point mutations was synthesized (Life Technologies) and amplified by PCR using Ku70Mut6E2-F and Ku70Mut6E2-R. Flanking regions were amplified by using Ku70-F/Ku70Mut6E1-R and Ku70Mut6E3-F/Ku70siR-R as primers and pICE-GFP-FLAG-Ku70siR-WT as a template. A fusion product was generated using Ku70-F and Ku70siR-R as primers and cloned into pICE as described for the wild-type Ku70siR, giving pICE-EGFP-FLAG-Ku70siR-Mut6E.

To generate pICE-HA-NLS-I-Ppol, a codon-optimized sequence coding for I-Ppol with an N-terminal HA tag, and the NLS of the SV40 large T antigen preceded by a start codon in a strong kozak context was synthesized (Life Technologies) and subcloned into pICE by HindIII–XhoI digestion.

Gene targeting
To tag the N terminus of *XRCC6* endogenously with GFP-FLAG, rAAV was produced by cotransfecting HEK293-AAV (Agilent Technologies) by pAAV-RC and pHelper (Agilent Technologies) and pAAV-Ku70-TC in equimolar ratio using Fugene HD (Promega) according to the manufacturer's instructions. In brief, 5×10^6 cells were seeded in 10-cm dishes and were transfected 24 h later in 7 ml DMEM, 5% FBS, and 2 mM glutamine to which 600 µl Opti-MEM containing 27 µl Fugene HD and 9 µg total of plasmids was added. After 24 h, cells were expanded in complete medium. 3 d after transfection, cells were collected in their growth medium, lysed by four cycles of freeze thaw, and centrifuged at 10,000 *g* for 10 min to isolate the virus-containing supernatants, which were stored at −80°C until use. Gene targeting was performed by infecting human RPE-1 cells (diploid), seeded the day before at 2×10^6 in 10-cm dishes, with 500 µl viral supernatant in 4 ml medium. 3 h later, a further 5 ml medium was added to each dish, and the cells were incubated with rAAV overnight. Cells were maintained in log-phase growth for 2 wk before sorting. Cells taken for sorting were trypsinized, filtered through 50-µm pores (CellTrics, Partec), and individually sorted in 96-well plates (µClear; Greiner) containing conditioned medium using a cell sorter (MoFlo; BD). After 10 d, cells showing correct nuclear GFP localization were identified using a microscope (Opera; PerkinElmer) and further expanded and validated by Western blotting.

Plasmid transfections and stable cell lines
Plasmid transfections were performed using Lipofectamine 2000 (Life Technologies) according to manufacturer's instructions. In brief, transfections were performed in 60-mm dishes containing confluent cells, in 2 ml DMEM, 5% FBS, and 2 mM glutamine to which 1 ml of the transfection mix in Opti-MEM containing 5 µg plasmid and 10 µl Lipofectamine 2000 was added. 5 h after transfections, media were refreshed with DMEM, 10% FBS, and 2 mM glutamine. To generate stable cell lines, cells were trypsinized the next day, seeded at low density, and selected with the appropriate antibiotic to isolate individual clones that were further validated by immunoblotting. G418 (Life Technologies) and puromycin (Sigma-Aldrich) were used at 500 µg/ml and 0.25 µg/ml, respectively, for cell selection and maintenance.

DNA–cellulose pull-down

3 d after the second round of transfection with siRNAs targeting Ku70, GFP-Ku70 wild type– and Mut6E-expressing cells were induced for 2 d with doxycycline before being collected by trypsination. Cell pellets were washed twice with PBS and resuspended in 500 µl DNA pull-down buffer (DPD buffer; 20 mM Tris-HCl, pH 7.5, 150 mM NaCl, and 0.2% Triton X-100) containing 1 mM AEBSF and cocktails of protease (cOmplete, Mini, EDTA free; Roche) and phosphatase inhibitors (cocktails I and II obtained from Sigma-Aldrich) supplemented with 0.3 mg/ml RNase A. After a 10-min incubation at 25°C, extracts were centrifuged 10 min at 13,000 RPM at 4°C, and supernatants were collected. For DNA pull-downs, 250 µg protein was incubated for 2 h on a rotating wheel at 4°C with 5 mg double-stranded DNA–cellulose matrix (Sigma-Aldrich) washed once in DPD buffer. After three washes in DPD buffer, DNA cellulose beads were boiled in 100 µl of loading buffer, and 20 µl of bound proteins was analyzed by immunoblotting.

Coimmunoprecipitations (IPs; co-IPs)

U2OS stably expressing GFP-FLAG only (clone 2; GFP) and U2OS Tet-On cells stably expressing doxycycline-inducible GFP-FLAG–tagged wild-type or Mut6E Ku70 resistant to siRNA (clone 8 and 7, respectively) were induced with doxycycline for 2 d. Cells were then pelleted and lysed in IP buffer (40 mM Tris-HCl, pH 7.5, 150 mM NaCl, 2 mM EDTA, 0.5% Triton X-100, 10% glycerol, and 1 mM DTT) containing 1 mM AEBSF and cocktails of protease (cOmplete, Mini, EDTA free) and phosphatase inhibitors (cocktails I and II) supplemented with 0.3 mg/ml RNase A. After a 10-min incubation at 25°C, extracts were centrifuged 15 min at 13,000 RPM at 4°C, and supernatants were collected. For co-IPs, 800 µg proteins in 500 µl IP buffer was incubated for 4 h on a rotating wheel at 4°C with 50 µl of magnetic anti-GFP beads (ChromoTek) washed once in IP buffer. After three washes in IP buffer, magnetic beads were boiled in 80 µl of loading buffer, and 40 µl of bound proteins was analyzed by immunoblotting on two gels, one for GFP blotting and one for Ku80 blotting. Ponceau staining was used as a loading control.

Clonogenic survival assays

The day before treatment, cells were seeded at known low densities into 6-well plates, with two cell dilutions per dose and three replicates per condition. Inhibitors were preincubated 1 h before treatments. X-ray treatments were performed using a calibrated RX-650 fitted with a 0.5-mm aluminum filter for soft x rays. 18 h after treatment, fresh medium was added to plates after two PBS washes. After 8–12 d, cells were stained with crystal violet, and the number of colonies per well was counted and normalized to the initial number of cells. For all experiments, data were normalized to the untreated conditions to take into account variations in plating efficiency.

Laser microirradiation

For each condition, 75,000 cells were seeded in glass-bottomed dishes (Willco Wells) 2 d before laser microirradiation. The day before irradiation, medium was refreshed with phenol red–free medium supplemented with 10 µM BrdU (Sigma-Aldrich). Laser microirradiation was performed with a confocal microscope (FluoView 1000; Olympus) and a 405-nm laser diode (6 mW with a SIM scanner) focused through a 60× U Plan S Apochromat/1.35 NA oil objective (Olympus). Laser settings (0.4-mW output for 50 scans) were used to generate DNA damage that was restricted to the laser path in a presensitization-dependent manner with minimal cellular toxicity.

Deconvolution and super-resolution microscopy

High-resolution pictures were acquired by imaging z stacks with a Deltavision PersonalDV (Applied Precision; 1,024 × 1,024 camera [CoolSNAP HQ2; Photometrics] and z stack of 0.2-µm intervals) or with a DeltaVision OMX V3 in conventional mode (Applied Precision; 512 × 512 cameras [Cascade II; Photometrics] and z stack of 0.125-µm intervals) both equipped with a 100× U Plan S Apochromat/1.40 NA oil objective (Olympus) and controlled with SoftWoRx software (Applied Precision). Deconvolutions were then performed with SoftWoRx in conservative mode. For structured illumination (3D-SIM) acquisitions, images were acquired on the Deltavision OMX V3 (512 × 512 Cascade II cameras, z stack of 0.125-µm intervals, and 75-mm SIM lens) and processed through SoftWoRx to generate super-resolution pictures. The OMX microscope was calibrated using fluorescent beads to align the different channels. For both high- and super-resolution microscopy, the different channels were acquired sequentially. For STED, pictures were acquired on a confocal microscope (TCS SP5 II; Leica) fitted with a STED module (592-nm depletion laser). Images were acquired with a 100× HCX Plan Apochromat/1.4 NA oil objective. For all micrographs, brightness and contrast were adjusted using ImageJ (National Institutes of Health), and

rotation and cropping were performed using Photoshop CS4 (Adobe). On all pictures in the paper, the white, green, and red scale bars correspond to 10, 1, and 0.2 µm, respectively.

Single-molecule counting

Molecule counting was performed using RPE-1 clone E4 (with both *XRCC6* alleles tagged with GFP-FLAG). Cells treated with 10 Gy of IR and postincubated for 5 min were preextracted with CSK+R and fixed with extra care to avoid light exposure. The OMX microscope was used to acquire 1-µm-thick stacks with a 0.2-µm interval; acquisitions were repeated 150 times to achieve full bleaching. On average, these stacks contained 30 individual foci. To minimize out of focus bleaching, only one cell was imaged per coverslip. Deconvoluted videos (SoftWoRx) were analyzed with ImageJ to plot the intensity for each focus during the acquisition time and in that way define the number of bleaching steps.

Quantification of Ku foci

For Ku foci quantification, cells were preextracted with CSK+R and processed for immunofluorescence. Deconvoluted pictures of >20 cells were acquired for each condition and submitted to automated focus detection by Volocity 6.0.1 (PerkinElmer) using different macros for the pictures generated by the PersonalDV and the OMX. To identify cells in S phase, cells were costained for proliferating cell nuclear antigen, a protein that accumulates in S phase and persists after CSK+R extraction. For normalization, the mean number of Ku foci in untreated cells was subtracted from the mean number of Ku foci in treated conditions.

Statistical analysis

When statistical analyses were required, an unpaired two-tailed t test was performed using Prism 4.0 (GraphPad Software) between pairs of conditions. Error bars on figures correspond to standard deviations. Quantifications are based on at least three independent experiments. In all figures, significant differences between specified pair of conditions, as judged by t test, are highlighted by asterisks (*, $P < 0.05$; **, $P < 0.01$; ***, $P < 0.001$). Nonlinear regressions were generated using Prism 4.0.

Online supplemental material

Fig. S1, related to Fig. 1, is a description and characterization of a mutant of Ku whose internal cavity charge has been reverted and use of this mutant to show that Ku foci observed with CSK+R preextraction are actually DNA-bound Ku. Fig. S2, related to Fig. 2, shows that Ku IRIF can be observed with our method in multiple human cell lines and on mitotic chromosomes. Fig. S3, related to Fig. 2, shows that CSK+R extraction preserves the organization of the nucleus and of repair factories and is compatible with analyzing HR events. Fig. S4, related to Fig. 3, shows that our method is also compatible with another super-resolution microscopy method, STED, that is used to map DNA ends into chromatin with increased accuracy. Fig. S5, related to Fig. 5, shows that the ATMi and DNA-PKi are used in our work at concentrations at which they are efficient and specific. Video 1, related to Fig. 2, is a 3D rendering of a whole U2OS nucleus showing that γ-H2AX foci colocalize with Ku foci when observed by high-resolution imaging. Video 2, related to Fig. 2, is a 3D rendering of a single γ-H2AX focus showing that γ-H2AX foci colocalize with Ku foci when observed by high-resolution imaging. Online supplemental material is available at http://www.jcb.org/cgi/content/full/jcb.201303073/DC1.

References

Altmeyer, M., and J. Lukas. 2013. To spread or not to spread—chromatin modifications in response to DNA damage. *Curr. Opin. Genet. Dev.* 23:156–165. http://dx.doi.org/10.1016/j.gde.2012.11.001

Arnaudeau, C., C. Lundin, and T. Helleday. 2001. DNA double-strand breaks associated with replication forks are predominantly repaired by homologous recombination involving an exchange mechanism in mammalian cells. *J. Mol. Biol.* 307:1235–1245. http://dx.doi.org/10.1006/jmbi.2001.4564

Bakkenist, C.J., and M.B. Kastan. 2003. DNA damage activates ATM through intermolecular autophosphorylation and dimer dissociation. *Nature*. 421:499–506. http://dx.doi.org/10.1038/nature01368

Bekker-Jensen, S., C. Lukas, R. Kitagawa, F. Melander, M.B. Kastan, J. Bartek, and J. Lukas. 2006. Spatial organization of the mammalian genome surveillance machinery in response to DNA strand breaks. *J. Cell Biol.* 173:195–206. http://dx.doi.org/10.1083/jcb.200510130

Berkovich, E., R.J. Monnat Jr., and M.B. Kastan. 2007. Roles of ATM and NBS1 in chromatin structure modulation and DNA double-strand break repair. *Nat. Cell Biol.* 9:683–690. http://dx.doi.org/10.1038/ncb1599

Bewersdorf, J., B.T. Bennett, and K.L. Knight. 2006. H2AX chromatin structures and their response to DNA damage revealed by 4Pi microscopy. *Proc. Natl. Acad. Sci. USA*. 103:18137–18142. http://dx.doi.org/10.1073/pnas.0608709103

Cheng, Q., N. Barboule, P. Frit, D. Gomez, O. Bombarde, B. Couderc, G.S. Ren, B. Salles, and P. Calsou. 2011. Ku counteracts mobilization of PARP1 and MRN in chromatin damaged with DNA double-strand breaks. *Nucleic Acids Res.* 39:9605–9619. http://dx.doi.org/10.1093/nar/gkr656

Ciccia, A., and S.J. Elledge. 2010. The DNA damage response: making it safe to play with knives. *Mol. Cell*. 40:179–204. http://dx.doi.org/10.1016/j.molcel.2010.09.019

Cramer, L.P., and T.J. Mitchison. 1995. Myosin is involved in postmitotic cell spreading. *J. Cell Biol.* 131:179–189. http://dx.doi.org/10.1083/jcb.131.1.179

de Vries, E., W. van Driel, W.G. Bergsma, A.C. Arnberg, and P.C. van der Vliet. 1989. HeLa nuclear protein recognizing DNA termini and translocating on DNA forming a regular DNA-multimeric protein complex. *J. Mol. Biol.* 208:65–78. http://dx.doi.org/10.1016/0022-2836(89)90088-0

Drouet, J., C. Delteil, J. Lefrançois, P. Concannon, B. Salles, and P. Calsou. 2005. DNA-dependent protein kinase and XRCC4-DNA ligase IV mobilization in the cell in response to DNA double strand breaks. *J. Biol. Chem.* 280:7060–7069. http://dx.doi.org/10.1074/jbc.M410746200

Dvir, A., L.Y. Stein, B.L. Calore, and W.S. Dynan. 1993. Purification and characterization of a template-associated protein kinase that phosphorylates RNA polymerase II. *J. Biol. Chem.* 268:10440–10447.

Falck, J., J. Coates, and S.P. Jackson. 2005. Conserved modes of recruitment of ATM, ATR and DNA-PKcs to sites of DNA damage. *Nature*. 434:605–611. http://dx.doi.org/10.1038/nature03442

Frit, P., R.Y. Li, D. Arzel, B. Salles, and P. Calsou. 2000. Ku entry into DNA inhibits inward DNA transactions in vitro. *J. Biol. Chem.* 275:35684–35691. http://dx.doi.org/10.1074/jbc.M004315200

Furuta, T., H. Takemura, Z.Y. Liao, G.J. Aune, C. Redon, O.A. Sedelnikova, D.R. Pilch, E.P. Rogakou, A. Celeste, H.T. Chen, et al. 2003. Phosphorylation of histone H2AX and activation of Mre11, Rad50, and Nbs1 in response to replication-dependent DNA double-strand breaks induced by mammalian DNA topoisomerase I cleavage complexes. *J. Biol. Chem.* 278:20303–20312. http://dx.doi.org/10.1074/jbc.M300198200

Gottlieb, T.M., and S.P. Jackson. 1993. The DNA-dependent protein kinase: requirement for DNA ends and association with Ku antigen. *Cell*. 72:131–142. http://dx.doi.org/10.1016/0092-8674(93)90057-W

Hickson, I., Y. Zhao, C.J. Richardson, S.J. Green, N.M. Martin, A.I. Orr, P.M. Reaper, S.P. Jackson, N.J. Curtin, and G.C. Smith. 2004. Identification and characterization of a novel and specific inhibitor of the ataxia-telangiectasia mutated kinase ATM. *Cancer Res.* 64:9152–9159. http://dx.doi.org/10.1158/0008-5472.CAN-04-2727

Iacovoni, J.S., P. Caron, I. Lassadi, E. Nicolas, L. Massip, D. Trouche, and G. Legube. 2010. High-resolution profiling of gammaH2AX around DNA double strand breaks in the mammalian genome. *EMBO J.* 29:1446–1457. http://dx.doi.org/10.1038/emboj.2010.38

Jackson, S.P., and J. Bartek. 2009. The DNA-damage response in human biology and disease. *Nature*. 461:1071–1078. http://dx.doi.org/10.1038/nature08467

Kim, J.A., M. Kruhlak, F. Dotiwala, A. Nussenzweig, and J.E. Haber. 2007. Heterochromatin is refractory to γ-H2AX modification in yeast and mammals. *J. Cell Biol.* 178:209–218. http://dx.doi.org/10.1083/jcb.200612031

Leahy, J.J., B.T. Golding, R.J. Griffin, I.R. Hardcastle, C. Richardson, L. Rigoreau, and G.C. Smith. 2004. Identification of a highly potent and selective DNA-dependent protein kinase (DNA-PK) inhibitor (NU7441) by screening of chromenone libraries. *Bioorg. Med. Chem. Lett.* 14:6083–6087. http://dx.doi.org/10.1016/j.bmcl.2004.09.060

Li, G., C. Nelsen, and E.A. Hendrickson. 2002. Ku86 is essential in human somatic cells. *Proc. Natl. Acad. Sci. USA*. 99:832–837.

Lieber, M.R. 2010. The mechanism of double-strand DNA break repair by the nonhomologous DNA end-joining pathway. *Annu. Rev. Biochem.* 79:181–211. http://dx.doi.org/10.1146/annurev.biochem.052308.093131

Mahaney, B.L., K. Meek, and S.P. Lees-Miller. 2009. Repair of ionizing radiation-induced DNA double-strand breaks by non-homologous end-joining. *Biochem. J.* 417:639–650. http://dx.doi.org/10.1042/BJ20080413

Miller, K.M., J.V. Tjeertes, J. Coates, G. Legube, S.E. Polo, S. Britton, and S.P. Jackson. 2010. Human HDAC1 and HDAC2 function in the DNA-damage response to promote DNA nonhomologous end-joining. *Nat. Struct. Mol. Biol.* 17:1144–1151. http://dx.doi.org/10.1038/nsmb.1899

Misteli, T., and E. Soutoglou. 2009. The emerging role of nuclear architecture in DNA repair and genome maintenance. *Nat. Rev. Mol. Cell Biol.* 10:243–254. http://dx.doi.org/10.1038/nrm2651

Nussenzweig, A., C. Chen, V. da Costa Soares, M. Sanchez, K. Sokol, M.C. Nussenzweig, and G.C. Li. 1996. Requirement for Ku80 in growth and immunoglobulin V(D)J recombination. *Nature*. 382:551–555. http://dx.doi.org/10.1038/382551a0

Ono, M., P.W. Tucker, and J.D. Capra. 1996. Ku is a general inhibitor of DNA-protein complex formation and transcription. *Mol. Immunol.* 33:787–796. http://dx.doi.org/10.1016/0161-5890(96)00030-2

Perrot, A., C. Pionneau, N. Azar, C. Baillou, F.M. Lemoine, V. Leblond, H. Merle-Béral, M.C. Béné, R. Herbrecht, S. Bahram, and L. Vallat. 2012. Waldenström's macroglobulinemia harbors a unique proteome where Ku70 is severely underexpressed as compared with other B-lymphoproliferative disorders. *Blood Cancer J.* 2:e88. http://dx.doi.org/10.1038/bcj.2012.35

Polo, S.E., and S.P. Jackson. 2011. Dynamics of DNA damage response proteins at DNA breaks: a focus on protein modifications. *Genes Dev.* 25:409–433. http://dx.doi.org/10.1101/gad.2021311

Roberts, S.A., and D.A. Ramsden. 2007. Loading of the nonhomologous end joining factor, Ku, on protein-occluded DNA ends. *J. Biol. Chem.* 282:10605–10613. http://dx.doi.org/10.1074/jbc.M611125200

Rogakou, E.P., D.R. Pilch, A.H. Orr, V.S. Ivanova, and W.M. Bonner. 1998. DNA double-stranded breaks induce histone H2AX phosphorylation on serine 139. *J. Biol. Chem.* 273:5858–5868. http://dx.doi.org/10.1074/jbc.273.10.5858

Rogakou, E.P., C. Boon, C. Redon, and W.M. Bonner. 1999. Megabase chromatin domains involved in DNA double-strand breaks in vivo. *J. Cell Biol.* 146:905–916. http://dx.doi.org/10.1083/jcb.146.5.905

Schermelleh, L., P.M. Carlton, S. Haase, L. Shao, L. Winoto, P. Kner, B. Burke, M.C. Cardoso, D.A. Agard, M.G. Gustafsson, et al. 2008. Subdiffraction multicolor imaging of the nuclear periphery with 3D structured illumination microscopy. *Science*. 320:1332–1336. http://dx.doi.org/10.1126/science.1156947

Shibata, A., S. Conrad, J. Birraux, V. Geuting, O. Barton, A. Ismail, A. Kakarougkas, K. Meek, G. Taucher-Scholz, M. Löbrich, and P.A. Jeggo. 2011. Factors determining DNA double-strand break repair pathway choice in G2 phase. *EMBO J.* 30:1079–1092. http://dx.doi.org/10.1038/emboj.2011.27

Soria, G., S.E. Polo, and G. Almouzni. 2012. Prime, repair, restore: the active role of chromatin in the DNA damage response. *Mol. Cell*. 46:722–734. http://dx.doi.org/10.1016/j.molcel.2012.06.002

Soutoglou, E., J.F. Dorn, K. Sengupta, M. Jasin, A. Nussenzweig, T. Ried, G. Danuser, and T. Misteli. 2007. Positional stability of single double-strand breaks in mammalian cells. *Nat. Cell Biol.* 9:675–682. http://dx.doi.org/10.1038/ncb1591

Taccioli, G.E., T.M. Gottlieb, T. Blunt, A. Priestley, J. Demengeot, R. Mizuta, A.R. Lehmann, F.W. Alt, S.P. Jackson, and P.A. Jeggo. 1994. Ku80: product of the XRCC5 gene and its role in DNA repair and V(D)J recombination. *Science*. 265:1442–1445. http://dx.doi.org/10.1126/science.8073286

Ting, N.S., Y. Yu, B. Pohorelic, S.P. Lees-Miller, and T.L. Beattie. 2005. Human Ku70/80 interacts directly with hTR, the RNA component of human telomerase. *Nucleic Acids Res.* 33:2090–2098. http://dx.doi.org/10.1093/nar/gki342

Ulbrich, M.H., and E.Y. Isacoff. 2007. Subunit counting in membrane-bound proteins. *Nat. Methods.* 4:319–321.

Walker, J.R., R.A. Corpina, and J. Goldberg. 2001. Structure of the Ku heterodimer bound to DNA and its implications for double-strand break repair. *Nature.* 412:607–614. http://dx.doi.org/10.1038/35088000

Wang, H., Z.C. Zeng, A.R. Perrault, X. Cheng, W. Qin, and G. Iliakis. 2001. Genetic evidence for the involvement of DNA ligase IV in the DNA-PK-dependent pathway of non-homologous end joining in mammalian cells. *Nucleic Acids Res.* 29:1653–1660. http://dx.doi.org/10.1093/nar/29.8.1653

Weinfeld, M., R.S. Mani, I. Abdou, R.D. Aceytuno, and J.N. Glover. 2011. Tidying up loose ends: the role of polynucleotide kinase/phosphatase in DNA strand break repair. *Trends Biochem. Sci.* 36:262–271. http://dx.doi.org/10.1016/j.tibs.2011.01.006